RSC Advances

ROYAL SOCIETY OF CHEMISTRY

www.rsc.org/advances

RSC Advances

Paper

Interactions of 1-hydroxypyrene with bovine serum albumin: Insights from multi-spectroscopy, docking and molecular dynamics simulation methods

Received 00th January 20xx,
Accepted 00th January 20xx

DOI: 10.1039/x0xx00000x

www.rsc.org/

Jing Zhang[a], Weixiao Chen[a,b], Bowen Tang[c], Wei Zhang[a], Linfeng Chen[a], Ying Duan[a], Yuxiu Zhu[a], Yaxian Zhu[d], Yong Zhang[a,e*]

The interaction between a typical PAH metabolite, 1-hydroxypyrene (1-OHP), and a transport protein, bovine serum albumin (BSA), has been investigated using fluorescence, UV-visible absorption (UV–vis), circular dichroism (CD) spectra, docking and molecular dynamics (MD) simulation methods under simulated physiological conditions (in Tris-HCl buffer, pH = 7.40). The experimental results suggested that the fluorescence quenching of BSA by 1-OHP occurred through a mixed static and dynamic quenching mechanism with a binding constant of 2.40×10^6 L mol^{-1} at 291 K. The thermodynamic parameters together with the docking and MD study revealed that Van der Waals forces dominate the formation of the 1-OHP-BSA complex. Applying Förster's non-radiation energy transfer theory, the binding distance of 1-OHP to BSA was calculated to be 2.88 nm. In addition, as confirmed by time-resolved fluorescence, UV–Vis, three-dimensional (3-D) fluorescence and CD spectra, high concentrations of 1-OHP induced conformational transitions of BSA, increasing the content of the α-helix of BSA and exposing its tryptophan residue to a more hydrophilic microenvironment. An inhibition test showed that 1-OHP strongly inhibits the binding constant of vitamin B_2 with BSA. A molecular docking study visualized the binding mode of 1-OHP with BSA. 1-OHP inserted into the binding pocket □B of BSA, leaving its hydroxyl group outside. Based on that, the MD study further unveiled the stability of 1-OHP-BSA complex and their dynamic binding modes, and clarified the contributions of each binding force component and the key residues to the binding process.

Introduction

Polycyclic Aromatic Hydrocarbons (PAHs) are widespread environmentally persistent organic pollutants [1]. Because of their highly hydrophobic and persistent characteristics, PAHs can accumulate in various organisms and pose a great potential hazard to human bodies and animal health on a global basis through exposure to various environmental phases, such as food chains, skin exposure and inhalation [2]. Upon entry into a human body, inactive parent PAHs are primarily metabolized by cytochrome P450 enzymes, forming a number of more active oxy-derivatives, including epoxides and hydroxyl compounds. These metabolites can bind to biomacromolecules, such as DNA and proteins, causing DNA damage and eventually leading to mutations [3, 4].

Serum albumin (ALB), the most abundant carrier protein in blood plasma, plays a fundamental role in the maintenance of the plasma colloid osmotic pressure and the binding and transportation of various endo- and exogenous compounds, such as fatty acids and drugs [5]. As has been reported, PAH metabolites can bind and form stable adducts with ALB [6]. These adducts can last about one month in human plasma and undergo no repair during the whole lifetime of the protein. Those PAH metabolites can then be transported to the target organs via blood circulation. As a result, the distribution, free concentration and disposition of PAH metabolites in vivo can be significantly affected by their binding to ALB. More importantly, the binding of PAH metabolites to ALB can result in adverse effects on the carrier protein, most likely by altering its structure or capturing its active binding sites. This may affect the normal biological functions of ALB and cause potential hazardous to organisms. For decades, studies have focused on developing methods to detect the level of PAHs or PAH derivatives-ALB adducts in human plasma and the correlation between these levels and the total exposure of PAHs [7]. However, to date, as an essential part to understand the disposition, transition and toxicity processes of PAH derivatives in vivo, the binding mechanism of PAH metabolites with ALB are not fully understood.

The interactions of ligands with ALB are of considerable interest for decades, especially in drugs and nanomaterials. There

[a] Address here. State Key Laboratory of Marine Environmental Sciences of China (Xiamen University), College of Environment and Ecology, Xiamen University, Xiamen, 361102, China
[b] College of Urban and Environmental Sciences, Peking University, Beijing 100871, China
[c] College of Pharmaceutical Sciences, Xiamen University, Xiamen 361102, China
[d] Department of Chemistry, College of Chemistry and Chemical Engineering, Xiamen University, Xiamen, 361005, China
[e] Zhangzhou Institute of Technology, Zhangzhou, 363000, China
†Electronic Supplementary Information (ESI) available:. See DOI: 10.1039/x0xx00000x

are plentiful literature precedents about their binding affinity with ALB, dominant binding forces, major binding sites on ALB, as well as the conformation transitions of ALB [8-10]. In contrast, to date, only the equilibrium constants [6] and binding site [11, 12] information of a few PAHs and their metabolites with ALB have been investigated. Some recent studies have sought a more detailed understanding on the mechanism of such a binding process. Wu et al. investigated the interactions of 1-naphthol and 2-naphthol with bovine serum albumin (BSA) using spectroscopy methods. Their results indicated that the two naphthol compounds form a complex with BSA through a hydrophobic interaction [13]. Ouyang et al. studied the interaction between 1-hydroxypyrene (1-OHP) and BSA with the presence of a surfactant, sodium dodecyl benzene sulfonate (SDBS), by combining fluorescence spectroscopy with UV-Visible absorption (UV-vis) spectra. Their findings suggested that the fluorescence of BSA was quenched by 1-OHP through a static quenching mechanism; the process was dominated by hydrogen bonding and Van der Waals forces [14]. However, it is plausible that the presence of SDBS can significantly affect the environment surrounding 1-OHP and BSA [15]. As a result, the findings cannot be applied to reflect the actual binding behavior, as discussed in our previous work [16]. Xu et al. studied the binding process of pyrene with BSA using spectroscopy methods and demonstrated that pyrene can form a 1:1 complex with BSA with a high affinity constant mainly through Van der Waals forces and hydrogen bonding, while inducing damage to BSA [17]. Although some progress has been made in the field, studies focusing on thoroughly integrated interactions of PAH metabolites with ALB in a more bio-relevant environment are still lacking. Knowledge on the binding modes between PAH metabolites and ALB is scarce. More importantly, the impact of PAH metabolites on the structure and biological functions of ALB are still unclear.

Spectroscopy methods, as a result of their sensitivity, relative ease of use and informational properties, are widely used to investigate ALB-ligand interactions. In recent years, theoretical calculation methods, such as molecular docking, have been applied to simulate the binding process of a ligand into the active site of a protein. Combinational use of experimental and docking research can provide more information on the interactions between ligands and ALB, such as references 18 and 19. In our previous work, we also employed multi-spectroscopy and docking method to study the interaction between inorganic mercury(II) and catalase (CAT) and predict their binding mode [20]. However, in most molecular docking studies, proteins are commonly treated as "rigid" molecules to save computational time, thus their conformations are not allowed to adjust during docking [21]. However, ALB is a very flexible protein, and its conformational changes induced by binding to ligands have been reported [17, 19]. Thus, molecular dynamics (MD) simulations, considering the flexibility of ALB, were deemed necessary to carry out to further simulate the dynamic interactions of ligands with ALB , as has been successfully used in references such as 9 and 22.

Therefore, in this study, based on our previous work [16, 23], 1-OHP was selected as a typical PAH metabolite, and BSA was selected as a model transport protein because of its well characterized physical properties, good stability and high similarity to human serum albumin (HSA). Multi-spectroscopy, in combination with the docking method, was employed to study the binding parameters (quenching mechanism, quenching constant, number of binding sites, binding distance and binding mode) of 1-OHP with BSA and the effects of the binding to 1-OHP on the structure and biological functions of BSA. MD simulations were also innovatively employed here to elucidate the stability of 1-OHP-BSA complex, and reveal the dynamic binding modes of 1-OHP with BSA at the atomic level. Their binding free energies were decomposed, and the contributions of each interaction force and key residues to the binding were further deciphered. To the best of our knowledge, an in-depth understanding of the interaction between PAH metabolites and BSA and their adverse impact on BSA was investigated here for the first time. The results obtained here will provide a detailed basic data to clarify the interaction mechanism of 1-OHP with BSA in vitro at both the molecular and atomic level, which is helpful to understand the toxicity effects of 1-OHP on the biological activity of the transport protein during the blood transportation process in vivo.

Experimental

Materials

BSA (purity > 99.5%), 1-OHP (purity > 99%) and vitamin B_2 (VB_2) (purity = 98%) were purchased from Sigma Chemical Company and were used without further purification. Tris-HCl buffer (0.05 mol L^{-1}, containing 0.10 mol L^{-1} NaCl) was used to keep the pH of the solution at 7.40. Stock solutions of 1-OHP (2.0×10^{-3} mol L^{-1} in ethanol) and BSA (4.0×10^{-5} mol L^{-1} in Tris-HCl buffer) were both kept in the dark at 4 °C for storage. All of the chemicals that were used were of analytical reagent grade. Milli-Q water was used throughout the study.

Methods

For all of the spectroscopy measurements, samples with different concentrations of 1-OHP and BSA were prepared by the sequential addition of 1-OHP and BSA (and VB_2 in the inhibition test) to a series of 10 mL colorimetric tubes and were diluted to a total volume of 10 mL with Tris-HCl buffer. The only exception was for circular dichroism (CD) measurements; these samples were diluted with Milli-Q water. All of the samples were performed in triplicate. After equilibration for 20 min, the spectra were measured.

UV-visible (UV-vis) absorption Spectra

UV-vis absorption spectra were measured in the range of 200 to 500 nm at room temperature (291 K) on a Cary60 UV spectrophotometer (Varian, USA). A quartz cuvette with a 1 cm path-length was used.

Fluorescence Measurements

Fluorescence measurements were carried out on a FLS920 steady / transient fluorescence spectrometer (Edinburgh, UK) that was equipped with a 150 W Xenon lamp. Samples were contained in a 1-cm quartz cuvette.

Steady-state quenching experiments were carried out with samples at 291, 308 and 318 K; these temperatures were maintained by placing the samples in a thermostatic water bath for 20 minutes for equilibration. Fluorescence measurements of each individual sample were taken shortly afterwards. The excitation wavelength was 282 nm, and the emission spectra were recorded from 290 to 400 nm. To correct the non-negligible inner filter effect (IFE) of 1-OHP on BSA fluorescence, all of the reported experimental fluorescence values were corrected by multiplying a factor of $10^{(Aex+Aem)/2}$, where A_{ex} / A_{em} is the absorption value of the BSA and 1-OHP mixture at the excitation/ emission wavelength of BSA [24].

Three-dimensional (3-D) fluorescence spectra at 291 K were measured with the initial excitation wavelength set at 200 nm with an increment of 5 nm, and the emission wavelength was recorded from 200 to 500 nm with increments of 5 nm. Thirty-one scanning curves were obtained. The excitation and emission slits were both set at 1 nm.

Time-resolved fluorescence intensity decays were also measured on a FLS920 fluorescence spectrometer at 291 K using the time-correlated single-photon counting (TCSPC) method. The excitation and emission wavelengths were set at 282 and 340 nm, respectively. Both excitation and emission slits were set at 10 nm. The lamp trigger delay was adjusted to 32 ns. The instrumental response function (IRF) was obtained by measuring a colloidal silica (Ludox AM-30, 30 wt. % suspension in water) solution. The fluorescence decay curves were analyzed with an iterative fitting program and a F900 that was provided by Edinburgh Instruments after deconvolution of the IRF. Typically, the reduced χ^2 value approaching 1 and a random distribution of weighted residuals indicates a good fit.

CD spectra

CD spectra (190-250 nm) were recorded using a Jasco-810 spectropolarimeter (Japan Spectroscopic, Japan) at 291 K. Three scans were obtained and averaged for each system. SELCON3 programs from the CDPro software package were used to calculate the secondary-structure content of BSA (http://lamar.colostate.Edu/~sreeram/CDPro/).

Molecular Docking Study

AutoDock 4.2.6 [25] implemented with a Lamarckian genetic algorithm (LGA) for a ligand conformational search was employed to perform the docking process. The 3-D structure of 1-OHP was drawn using Gauss View 5.0 and was optimized with Gaussian 09 [26]. The native structure of BSA was downloaded from the Protein Data Bank (PDB ID: 4F5S) [27]. The docking process and docking parameters were set up as described in a previous literature [28]. The docking results presented here were analyzed using PyMOL software [29].

MD simulations

MD simulations were performed on the 1-OHP-BSA complex structure from docking using Amber14 and AmberTools15 software package [30] following the reported protocols [31]. The atomic partial charges for 1-OHP were computed by the electrostatic potentials (ESP) method at the level of B3LYP and the 6-31G(d) basis set using Gaussian 09 package [26]. The Amber ff14SB force field and the general Amber force field (GAFF) [32] were used to establish force field parameters for BSA and 1-OHP, respectively. The complex was neutralized by adding 35 Na^+ ions, and then solvated in a truncated octahedron box surrounded by no less than 8 Å TIP3P water molecules. The resultant system was composed of approximately 60,897 atoms. The system was then optimized by energy minimization using steepest descent and conjugated gradient method, and then gradually heated to 300 K for 200 ps. Finally, the system was equilibrated in an isothermal-isobaric (NPT) ensemble with unconstrained MD simulations for first 50 ps and unconstrained MD simulations for further 50 ns. During above steps, the long range electrostatic interactions were calculated by the particle mesh Ewald (PME) method using a 8 Å nonbonded cutoff, while The SHAKE algorithm was applied to constrain all covalent bonds involving hydrogen atoms. The MD simulation results were analyzed using the cpptraj program in the AmberTools 15 package, PyMOL software and the Visual Molecular Dynamics (VMD) 1.9.2. Based on the obtained 50 ns MD trajectories, the binding free energy between 1-OHP and BSA was decomposed for every 5.0 ns MD simulation using the molecular mechanics Poisson-Boltzmann solvent accessible surface area (MM-PBSA) method. The total binding free energy and their decomposition were calculated as described by Ghadari et al [33], and Cui et al [34].

Results and Discussion

Characterization of the interaction of 1-OHP with BSA

The intrinsic fluorescence of BSA is very sensitive to its local microenvironment and can be easily affected when binding to small molecules [35]. The fluorescence quenching method was thus employed here to clarify the binding mechanism between BSA and 1-OHP and obtain their binding constant. The fluorescence spectra of BSA in the presence of 1-OHP at various concentrations are illustrated in Fig. 1. As shown in Fig. 1, BSA has an intrinsic fluorescence peak at approximately 340 nm, which is mainly attributed to its tryptophan (TRP), tyrosine (TYR) and phenylalanine (PHE) residues [24]. With the addition of 1-OHP, a steady quenching of the fluorescence intensity of BSA can be observed. Besides, the quenching effect was mainly dependent on the concentration of 1-OHP.

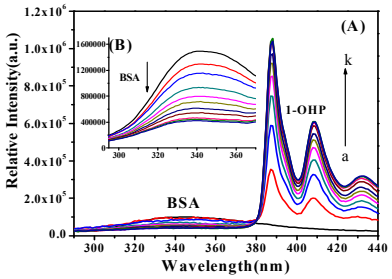

Fig. 1 Fluorescence emission spectra of 5.0 ×10^{-6} mol L^{-1} BSA in the presence of 1-OHP at 291 K. $C_{1\text{-OHP}}$ (a-k): (0, 0.1, 0.2, 0.3, 0.4, 0.5, 0.6, 0.7, 0.8, 0.9, 1.0) ×10^{-5} mol L^{-1}; (A) Ex slit = Em slit =1 nm; (B) Ex slit = Em slit = 2 nm.

The fluorescence quenching of BSA by 1-OHP may be caused by a ground-state complex formation or the occurrence of collisional encounters during the excited state between them. To determine the quenching mechanism between BSA and 1-OHP, the fluorescence lifetimes of pure BSA and 1-OHP-BSA systems were measured separately. A decrease in the fluorescence lifetime (τ_f) of BSA with increasing 1-OHP concentration was observed (Fig. S1), which offers evidence that the dynamic quenching process has occurred [24]. Moreover, the Stern-Volmer plot (using Eq. S1) of the fluorescence intensities of BSA at 340 nm clearly curves toward the y-axis (Fig. 2), as observed in many instances [36]; this result qualitatively insinuated a mixed quenching process was involved in the interaction of 1-OHP with BSA[24].

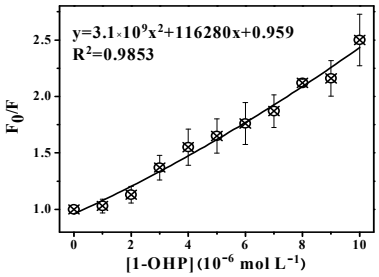

Fig. 2 Stern–Volmer plot for the quenching of BSA by 1-OHP at 291K

To extract a more quantitative view of the mixed quenching mechanism, the data were analyzed using the Stern-Volmer equations (Eq. S1-S2) according to references [24] and [36]; the dynamic quenching constant K_D of 1-OHP and BSA was determined to be 4.14×10^4 L mol^{-1}, with the static quenching constant K_S equal to 7.48 ×10^4 L mol^{-1}. The results suggest a mixed static and dynamic quenching mechanism for the quenching process of 1-OHP on BSA, while static quenching is dominant.

For the static quenching dominant process, the double-logarithm equation can be used to determine the number of binding sites (n) and the binding equilibrium constant (K_b) between 1-OHP and BSA, as previously described [37]. As calculated from the plots of log (F_0 / F − 1) versus log[Q] for 1-OHP and BSA (Fig. S3), the values of K_b and n at 291, 308, 318 K for the 1-OHP-BSA system are listed in Table 1.

As shown in Table 1, the K_b and n values decrease regularly with increasing temperature, indicating that higher temperature decreased the formation of the 1-OHP-BSA complex. Furthermore, at 291 K, the n value approximately equalled 1, and the large K_b value of 2.40×10^6 L mol^{-1} suggested that 1-OHP has a strong affinity to BSA with one specific binding site. The K_b value is on the same order of magnitude with that of other PAH-ALB, such as references [38] and [6]. Meanwhile, the K_b value is as large as that obtained for the interaction of ALB with various bioactive substances, such as nobiletin (3.66 × 10^6 L mol^{-1}), chrysin (1.20 × 10^6 L mol^{-1}) and kaempferol (2.58 × 10^6 L mol^{-1}) [8]. This indicated that 1-OHP can bind with the transport protein as strongly as these bioactive substances that are important for organism functioning. Moreover, the K_b value was similar or even larger compared to that of the pyrene-BSA complex reported by Xu et al. (2.63×10^6 L mol^{-1}) [17] and Tsukamoto and Hikida (1.00×l0^6 L mol^{-1}) [39]. This is in accordance with the report that with the increase in the electrophilic properties of PAH molecule caused by the hydroxyl group, the affinity of some PAHs metabolites towards biomacromolecules increases compared with their parent PAHs [6]. It is known that the binding constant of ligands to albumin is an important indicator of the activity of these substances in vivo [40]. Thus, the result obtained here warns that when considering the importance of the toxicity of hydrophobic pollutants and their structurally similar substances (i.e., drugs), it is crucial to take into account their metabolites [16].

Types of interaction force

The interaction forces between biological macromolecules and small organic molecules mainly include hydrogen bonds, van der Waals' interactions, electrostatic forces and hydrophobic interactions [41]. Enthalpic change (ΔH) together with entropic change (ΔS) can provide insights into the type of interaction forces dominated in the binding process. Thus, the thermodynamic measurements were employed to help determine the major interaction forces that were present in the binding process of 1-OHP with BSA. Assuming that ΔH does not vary over the experimental temperature range, thermodynamic parameters can be calculated using a Van't Hoff analysis and thermodynamic equations [42]. The ΔH and ΔS values were calculated as the slope and ordinate from the LnK_b vs. 1/T plot (Fig. S4), respectively. All of the relevant thermodynamic parameters of BSA and 1-OHP are listed in Table 1. The negative value of free-energy change (ΔG) revealed that the interaction of 1-OHP and BSA was spontaneous. Because ΔH < 0 and ΔS < 0, Van der Waals or hydrogen bonding forces must be the main interaction forces involved in the binding process of 1-OHP with BSA [41, 43].

Table 1 Thermodynamic properties of the interaction between 1-OHP and BSA

T (K)	K_b (L mol^{-1})	n	R^a	ΔG (KJ mol^{-1})	ΔS (J mol^{-1} K^{-1})	ΔH (KJ mol^{-1})
291	2.40×10^6	1.23	0.990	-35.39		
308	3.43×10^5	1.05	0.997	-33.08	-136.02	-74.97
318	1.82×10^5	0.99	0.981	-31.72		

[a] R is the correlation coefficient

Binding distance from BSA to 1-OHP

Fluorescence resonance energy transfer (FRET) is primarily used to measure the molecular distance of the donor–acceptor complex. Because the absorption spectrum of 1-OHP provides sufficient overlap with the fluorescence emission spectrum of BSA (Fig. 3), the energy transfer from BSA to 1-OHP can occur with a high probability according to Forster's dipole-dipole non-radioactive energy transfer theory [44]. The binding distance between the TRP residue of BSA and 1-OHP was thus investigated using FRET. After fitting data to Eq. (S3)-(S5), all of the parameters values related to energy transfer are calculated and listed in Table S1.

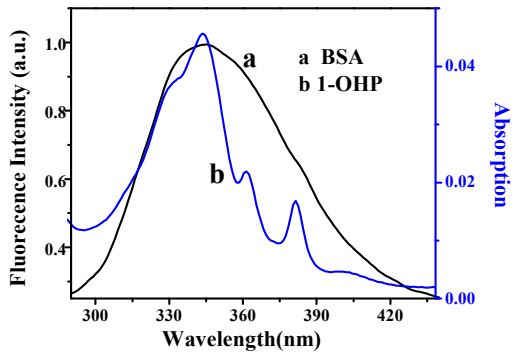

Fig. 3 Overlap of UV–vis spectrum of 1-OHP (b) with the fluorescence emission spectrum of BSA (a). $C_{BSA} = C_{1\text{-}OHP} = 5.0\times10^{-6}$ mol L^{-1}

As calculated, the energy transfer efficiency (E) of BSA to 1-OHP is 0.4. The distance from the TRP residue of BSA to 1-OHP (r) is 2.88 nm, which is less than 7 nm; it confirms that there is a high probability of energy transfer from BSA to 1-OHP. Furthermore, the presence of a static quenching mechanism for the interaction between 1-OHP and BSA is demonstrated again [45].

Fluorescence lifetime measurements

The fluorescence lifetime measurements are highly sensitive for detecting the excited-state interactions and measuring the possible micro-environment changes of the protein [24]. To confirm that the binding of 1-OHP induces the micro-environmental changes of BSA, the time-resolved fluorescence decays of BSA in the presence of 1-OHP were measured with the corresponding parameters displayed in Table 2.

In Table 2, the observed curves for free BSA and the 1-OHP-BSA complex fit exponentially with good χ^2 values. For free BSA, two lifetime components of 3.16 ns and 6.56 ns were obtained. In contrast, three lifetime components were detected with the addition of 1-OHP, which suggests a higher system complexity. The lifetimes of the three components remain stable at a low 1-OHP concentration and then increase slightly at 5.0×10^{-6} mol L^{-1} of 1-OHP and continue to grow with the addition of 1-OHP. The contribution intensities of the short lifetimes of τ_1 and τ_2 increase with increasing 1-OHP concentration, while the contribution of the long lifetime τ_3 displays a decreasing trend.

Table 2 Fluorescence decay parameters for BSA in the absence and presence of different amounts of 1-OHP. $C_{BSA}= 5.0\times10^{-6}$ mol L^{-1}

$C_{1\text{-}OHP}$ (mol L^{-1})	τ_1 (ns)	τ_2 (ns)	τ_3 (ns)	α_1 (%)	α_2 (%)	α_3 (%)	τ_f (ns)	χ^2
0	-	3.16	6.56	-	17.04	82.96	5.98	1.086
2.0×10^{-6}	0.11	3.05	6.45	5.75	19.94	74.31	5.41	1.250
4.0×10^{-6}	0.11	3.29	6.63	7.61	38.63	53.76	4.79	1.091
5.0×10^{-6}	0.17	3.20	6.56	8.92	41.34	49.74	4.59	1.169
6.0×10^{-6}	0.52	3.56	7.21	8.64	56.96	34.40	4.41	1.137
8.0×10^{-6}	0.68	3.80	8.92	10.97	70.64	18.39	4.39	1.039
1.0×10^{-5}	0.62	3.59	8.58	11.86	68.19	19.95	4.15	1.135

Short lifetimes of BSA at 0.3–0.4 ns and 2–3.5 ns have been commonly considered to be associated with the intrinsic property of the TRP structure, while the longer lifetime at about 6 ns is attributed to the interaction between the TRP residue (s) and the surrounding environment. Additionally, the relative contribution of each component depends on the number of emitting TRP residues or/and on the type of interaction occurring between TRP residues and the surrounding environment [46]. Based on both the increasing trend of longer lifetime τ_3 and the changes for each component contributions, it is therefore evident that the interaction of 1-OHP and BSA altered the protein structure near the TRP residues of BSA and changed the micro-environment around the TRP residues. The continual decreasing of the lifetimes indicates that higher concentrations of 1-OHP can induce greater structural alteration of BSA. The same phenomenon is also reported in [19].

Conformation transition of BSA with 1-OHP

The UV-vis absorption, 3-D fluorescence and CD spectroscopy results are discussed in the following sections, focusing on how the interaction impacts the structure or micro-environment of BSA.

UV-Vis absorption spectroscopy UV-vis absorption spectroscopy is a simple method that can be used to reveal information about the complex formation and structure changes of BSA. The UV–Vis absorption spectra of BSA with various concentrations of 1-OHP are obtained by subtracting the corresponding spectra of free 1-

OHP from the 1-OHP-BSA complex system (Fig. 4). As shown in Fig. 4, BSA has two major absorption peaks: one lies about 210 nm, designating its secondary structure with a majority representing the α-helix structure of BSA [47]; and the other at 278 nm, reflecting the aromatic amino acids (TRP, TYR, PHE, mainly TRP) and the transformation of their micro-environment [48]. With the continuous addition of 1-OHP, the fluorescence intensity of the peak at about 210 nm increases, suggesting an increase of the α-helix content of BSA. The intensity of the peak at 278 nm increases with a 2-nm red shift, which indicates a decrease in the hydrophobicity of the micro-environment of TRP and other residues and the formation of the 1-OHP-BSA complex [49]. Thus the static quenching process involved is corroborated again. [48]

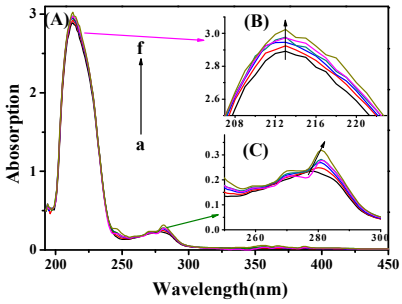

Fig. 4 UV absorption spectra of BSA with different concentrations of 1-OHP (A); (B) and (C) are the magnified illustrations of the peaks of BSA at approximately 212 and 278 nm. C_{BSA}= 5.0×10^{-6} mol L^{-1}; $C_{1\text{-}OHP}$ (a-f) = (0, 0.2, 0.4, 0.6, 0.8, 1.0) ×10^{-5} mol L^{-1}

3-D fluorescence spectroscopy 3-D fluorescence spectroscopy provides comprehensive fluorescence information of the ligand-BSA complex. Therefore, 3-D fluorescence spectra and the contour plot of BSA have been measured with and without 1-OHP (Fig. 5) to further investigate the micro-environmental transition of BSA. Corresponding parameters are listed in Table 3.

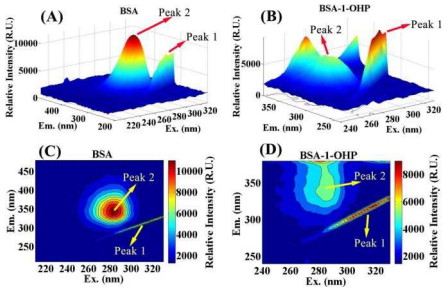

Fig. 5 3-D fluorescence spectra of BSA (A), 1-OHP-BSA system (B) and the 3-D contour map counter plots of BSA (C), 1-OHP-BSA system (D). C_{BSA} = $C_{1\text{-}OHP}$ = 5.0×10^{-6} mol L^{-1}

Peak 1 in Fig. 5 is the Rayleigh scattering peak (λ_{ex} = λ_{em}). The peak intensity increases with the addition of 1-OHP, which suggests the formation of the 1-OHP-BSA complex, causing a larger macromolecule diameter and enhancing the scattering effect [50]. Peak 2 (λ_{ex} = 282 nm, λ_{em} = 341 nm) in Fig. 5 primarily reveals the intrinsic fluorescence of TRP residues [51]. Its fluorescence intensity exhibits a drastic decrease from 11620 to 5923 with the addition of 1-OHP and a red shift of about 3 nm at the maximum emission wavelength, suggesting that the TRP residues of BSA exposed to a less hydrophobic micro-environment [52].

Circular dichroism (CD) spectroscopy CD spectroscopy [53] was further performed to quantitatively study the secondary structural changes of BSA by 1-OHP. As shown in Fig. 6, for the CD spectra of pure BSA, two negative peaks are observed at approximately 208 and 220 nm, both of which are the characteristic of the α-helix structure of BSA [35]. With the increasing concentration of 1-OHP, the intensity of the two negative peaks of 1-OHP-BSA increased, inferring considerable changes in the secondary structure of BSA with increasing helical stability. After fitting the CD data into CDPro software, the quantitative analysis results of the secondary structure contents of each system are listed in Table 4.

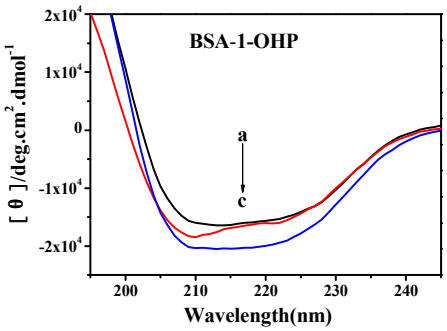

Fig. 6 CD spectra of the 1-OHP-BSA systems at different molar ratios of 1-OHP to BSA. $C_{1\text{-}OHP}$: C_{BSA} (a–c) = 0:1; 1:1; 10:1

In Table 4, pure BSA is mainly α-helices, with a percentage of 50.9%, which is in good agreement with previously published literature [19]. Compared with the results of pure BSA, the secondary structure contents of BSA exhibit a steady change in response to the increasing ratio of 1-OHP. With a molar ratio of 1-OHP to BSA at 10:1, there is approximately a 7% increase of α-helices and a 11% increase of turn, with an accompanying decrease of β-sheets and random coil contents of 30% and 12%, respectively. Therefore, our results suggest that the addition of 1-OHP obviously leads to secondary structural alterations of BSA, mainly by increasing the helical stability of BSA and breaking down the β-sheet and random coils structure. This may be a result of the formation of the 1-OHP-BSA complex, as demonstrated in [54]. In addition, the greater structural alteration of BSA that was induced by higher concentrations of 1-OHP was confirmed again.

RSC Advances

Paper

Table 3 3-D spectral characteristic parameters of the BSA and 1-OHP-BSA systems

Peaks	BSA			1-OHP-BSA		
	Peak position λ_{ex} / λ_{em} (nm/nm)	Stokes shift Δλ (nm)	Intensity	Peak position λ_{ex} / λ_{em} (nm/nm)	Stokes shift Δλ (nm)	Intensity
Peak1	200/200-330/330	0	1202-16100	240/240-330/330	0	2021-19030
Peak2	282/341	59	11620	284/344	60	5923

Table 4 Secondary structural alterations of BSA as determined by SELCON

$C_{1\text{-}OHP}$ / C_{BSA}	α-Helix (%)	β-Sheet (%)	Turn(%)	Random coil (%)	RMSD [a]
0:1	50.9	11.6	13.1	24.5	0.101
1:1	51.2	9.8	13.9	25.3	0.239
10:1	54.5	8.2	14.6	22.7	0.083

[a] RMSD is the root-mean-square deviation

Inhibition effects of 1-OHP on the physiological function of BSA to transport Vitamin B_2

From the results above, 1-OHP can form strong interaction with BSA, and induce the structural changes of BSA. Thus the normal biological function of BSA may also be affected by the accumulation of 1-OHP, such as the binding and carrying capacity of BSA [55]. To reveal the effects of 1-OHP on the transport functions of BSA, the inhibition test of 1-OHP on the binding ability of BSA with VB_2 was performed using the fluorescence quenching method. Fitting to the double-logarithm equation [56], the calculated K_b and n values for the VB_2-BSA systems are listed in Table 5.

With the addition of 1-OHP, the K_b and n values of BSA and VB_2 decrease significantly compared with those without 1-OHP. 1-OHP at 1.0×10^{-5} mol L^{-1} reduces the binding constant of VB_2 with BSA by nearly two orders of magnitude and decreases the number of binding sites of VB_2 in BSA from 1.23 to 0.65. To the best of our knowledge, the binding sites of VB_2 on BSA haven't been clearly clarified yet[57-60]. Even so, the competition interaction between 1-OHP and VB_2 with BSA cannot be excluded. Moreover, according to Zhang et al[61] and Chen et al[62], small molecules can change the conformation of BSA after binding to BSA, making the conformation unfavorable for the binding of VB_2 to BSA. Since the addition of 1-OHP alters the secondary structure of BSA and changes the microenvironment near Trp residues, the conformations of BSA after damaged by 1-OHP may also become unfavorable for binding to VB_2 [61]. Thus the effect of the conformational changes of BSA on the binding of VB_2 on BSA should not be neglected. In summary, the accumulation of 1-OHP could damage the physiological function of BSA possibly by altering its conformation and occupying its active binding sites, which may lead to potential danger for organisms.

Table 5 K_b and n values of BSA-VB_2 systems in the absence and presence of different concentrations of 1-OHP at 291 K. $C_{BSA} = 4\times10^{-6}$ mol L^{-1}; C_{VB2} = (0, 4, 8, 1.2, 1.6, 2.0) $\times10^{-5}$ mol L^{-1}; $C_{1\text{-}OHP}$ (10^{-5} mol L^{-1}) = a, 1; b, 2

System	K_b (L mol^{-1})	n	R [a]
VB_2-BSA	5.34×10^5	1.23	0.996
VB_2-1-OHP-BSAa	5.73×10^4	0.95	0.994
VB_2-1-OHP-BSAb	7.64×10^2	0.65	0.989

[a] R is the correlation coefficient

Binding site for 1-OHP in BSA: molecular docking study

In order to know more information about the binding site location and binding mode, theoretical calculation methods could be used here. Because of the promising results in searching for the binding location of ligands on BSA [28, 20], the AutoDock blind docking method has been employed to seek the preferred binding location of 1-OHP in BSA and to corroborate the experimental observations. Out of the 25 conformers that were obtained, the conformer with the lowest binding free energy (-28.55 KJ mol^{-1}) was used for further analysis.

Binding energy and binding constant For the selected conformer, the binding constant with BSA is calculated to be 3.50×10^5 L mol^{-1}. The high binding constant again indicate a strong interaction between 1-OHP and BSA. It is worth noting that these results are slightly different from the results of thermodynamic and spectroscopy experiments (ΔG = -29.95 kJ mol^{-1}, $K_b = 2.40\times10^6$ L

mol^{-1}). This may be caused by the difference between the X-ray structure of BSA from crystals and that of the aqueous system used in the experimental study, resulting in different microenvironments around the ligand [63, 64].

Binding sites and binding distance Given the fluorescence quenching result, only one binding site of 1-OHP is found in the BSA molecule. Fig. 7a illustrates that 1-OHP is bound to the subdomain ⅡB of BSA in accordance with the point that the subdomain ⅡB is a specific binding site for PAH epoxides [12], as well as being the primary binding site for some other hydrophobic ligands [28].

The distances between 1-OHP and the two TRP residues, TRP134 and TRP213, are measured to be 1.2 nm and 2.5 nm, respectively. Such close proximity highly supports the possible energy transfer from TRP residues to the 1-OHP molecule, as revealed earlier in the results of the energy transfer study.

Binding mode and forces As shown in Fig. 7b, the hydrophobic parent part of 1-OHP inserts into the cavity of BSA with its -OH substituent exposed to the surface of BSA. This resembles the binding behaviour of drug molecules with a hydrophilic group, such as a carboxyl group and a hydroxyl group [65, 66]. A hydrogen bond is observed between -OH and GLU182 with a bond length of 1.9 Å. Both hydrophobic amino acid residues (TRP160, PRO117 and ILE181) and charged / polar residues (GLU182, ARG185 and LYS114) appear within 4 Å of 1-OHP (Fig. 7c). These results suggest that in addition to hydrogen bonds, contributions of hydrophobic, Van der Waals and electrostatic force should not be dismissed when 1-OHP interacts with BSA [28], which agrees with the results from the thermodynamic study that hydrogen bonds and Van der Waals forces may be dominant in the binding process.

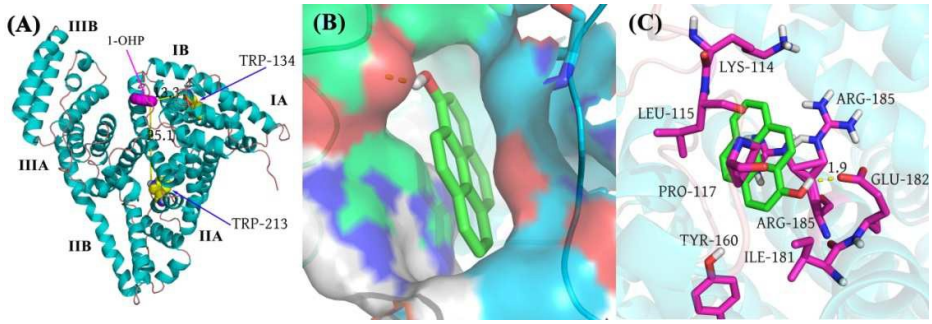

Fig. 7 Docking results of the 1-OHP-BSA system: (A) Binding site and distance from TRP residues to 1-OHP, (B) Binding mode, (C) neighboring amino acids within a distance of 4 Å approximately 1-OHP (the hydrogen bond between 1-OHP and GLU182 is shown as yellow dots). (Read more about the colors in supporting information)

Molecular dynamic simulations

In order to gain deeper understanding of the interaction process, the lowest energy structure of 1-OHP-BSA complex resulting from the docking process was selected as the initial structure for 50 ns MD simulations.

Root mean square deviations (RMSD) To analyse the stability of the 1-OHP-BSA complex, the RMSD values of the backbone atoms of BSA and 1-OHP from their positions in the initial structures were investigated, as described by Cui et al[34]. As shown in Fig. 8 that the RMSD of BSA in the presence of 1-OHP reaches equilibrium with an average value of 3 Å after about 12 ns, and the RMSD of 1-OHP remains smooth overtime. It suggests that the complex system becomes equilibrated and stable after 12 ns, while 1-OHP is in an equilibrium state during the simulation period [67].

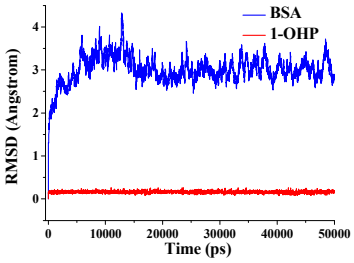

Fig. 8 Time evolutions of the backbone RMSD of BSA (blue line) and 1-OHP (red line) in MD simulations.

Physicochemical parameters such as the total energy and potential energy were also calculated and presented in Fig. S5. The stable total energy and potential energy with smooth curves also indicate that the system reaches stability[68]. Meanwhile, the evolution of the conformation of the complex over time was displayed using VMD software, which shows that 1-OHP is always immersed in the IB subdomain of BSA. These results further confirm that the molecular docking result for the binding location of 1-OHP in BSA is credible.

Analysis of dynamic binding models Since the MD simulation considers the flexibility of BSA, to further reveal the dynamic interactions between 1-OHP and BSA, the snapshot conformations of 1-OHP-BSA complex at 15, 20, 30 and 40 ns were selected and analysed. As shown in Fig. 9, for the four snapshots, 1-OHP is orientated differently in the subdomain IB of BSA, surrounded by different residues. The conformational changes of 1-OHP can be clearly seen in the overlapping map of the four snapshots, shown in Fig. S6a. The average root mean square fluctuation (RMSF) values of above 6 Å for each atom of 1-OHP (Fig. S6b) confirm that the position of 1-OHP shifts dynamically from its initial position. Using AmberTools15, the conformational changes of 1-OHP at four snapshots were further calculated and listed in Table S2. As shown, from 15 ns to 40 ns, the no-fit RMSD of 1-OHP fluctuates obviously; the angle of -OH group of 1-OHP rotates from 102.12° to 104.66°; and the dihedral angle between the -OH group and the fused ring group of 1-OHP rotates dramatically from -170.77° to 178.55°.

The position shifts and the rotations of the -OH group of 1-OHP may induce different interaction modes of 1-OHP with the nearby residues overtime, such as the different hydrogen bonds and cation- π interactions formed overtime. For instance, in Fig. 9, 1-OHP forms a hydrogen bond with GLU182 and LYS114, at 15 ns and 30 ns, respectively. Whereas no hydrogen bond is detected at 20 ns and 40 ns.

Since the hydrogen bond is closely related to the electrostatic interactions of 1-OHP to BSA[34], the occurrence and geometry of the hydrogen bonds between 1-OHP and BSA during the simulation time were further determined and analysed using hbond program from AmberTools15.

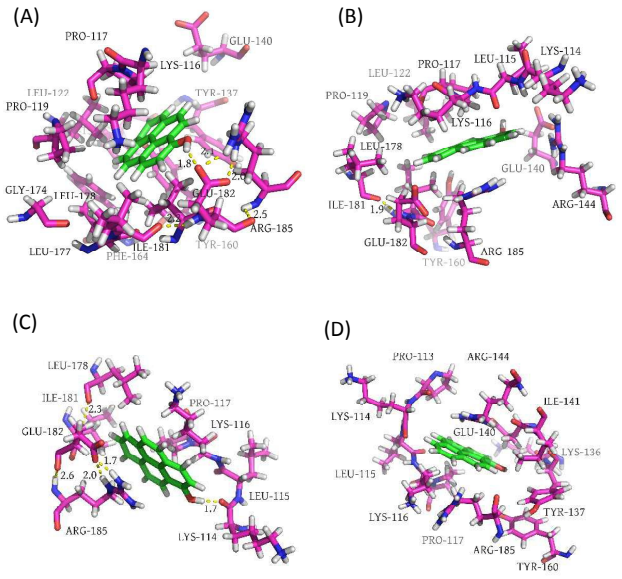

Fig. 9 Binding modes of 1-OHP with BSA at 15 ns (A), 20 ns (B), 30 ns (C), and 40 ns (D) in the MD simulation (the hydrogen bonds between 1-OHP and GLU182, GLU182 and other residues are shown as yellow dots). Read more about the colors in supporting information.

As listed in Table S3, in agreement with the docking result, two hydrogen bonds are formed between the phenol OH of 1-OHP and OE1, OE2 group of GLU182 with an average distance of 2.63 Å and 2.64 Å. However, the two hydrogen bonds only occupy 34.42% and 17.24% of the simulation time, respectively. Meanwhile, other hydrogen bonds are formed between 1-OHP with GLU140, TYR160, LYS114, LEU115, PRO117 and PRO113 residues with low occupancies of all below 3%. The results confirm that the hydrogen bonds between 1-OHP and residues of BSA are not stable. The low occupancy of hydrogen bonds may be caused by that the solvent molecules penetrating into the binding site may attack on the hydrogen bonds, resulting in the weakness of hydrogen bond stability, as reported previously[31]. Thus the hydrogen bond forces cannot play an important role in the binding process. Moreover, as illustrated in Fig. 9, during the most simulation time, there exit strong cation- π interactions between the large π system from 1-OHP and the positively charged nitrogens from the side chain of nearby residues; the cation-π interactions formed between 1-OHP and ARG185 at 20 ns and 30 ns, or ARG144 at 40 ns (Fig. S7). Comparing to the former hydrogen bonds forces, the cation- π interactions may be more important for 1-OHP binding to BSA. Moreover, in the simulations, some hydrophobic amino acid residues (TRP160, PRO117 and ILE181) and charged / polar residues (GLU182, ARG185 and LYS114, LYS116) always appear within 5 Å of 1-OHP. This result indicates that both hydrophobic and polar forces play an important role in the binding of 1-OHP to BSA.

Besides the interactions between 1-OHP and residues, the conformation of BSA at four snapshots were also calculated and lists in Table S4. The secondary structures of the BSA during each 500 frames show no obvious changes, because of BSA being in the equilibrium state. Even so, it is worth to note the changes of the residues induced by the binding to 1-OHP. As shown in Fig. 9, during the simulation, after 1-OHP come into this binding site, the nearby residues change its conformation and position for more stable state of complex system. For instance, compared the snapshot at 30 ns to that at 15 ns, it is obvious to see that at 15 ns the OE1, OE2 atom of GLU182 formed a hydrogen bond with the HE, HH2 atom of ARG185, with corresponding bond lengths of 2.0 Å and 2.1 Å. Whereas, at 30 ns, the orientation of GLU182 changes significantly; the OE2 atom of GLU182 formed two hydrogen bonds with the HE, HH2 atomic of ARG185, with closer distance of 2.0 Å and 1.7 Å. Thus the conformation of GLU182 becomes more stable, and its surrounding microenvironment also changes. The position, orientation and microenvironment changes of the residues induced by binding to 1-OHP further confirm the UV-vis and CD spectra result that the interactions with 1-OHP induce the structural and microenvironmental changes of BSA.

Binding free energy analysis

To gain further insight into the forces involved in the binding process of 1-OHP with BSA, the total binding free energy was decomposed and analysed using MM-PBSA methods. The MM-PBSA

binding free energy calculations were carried out for the 500 snapshots of every 5 ns MD simulation. The contributions of each component are shown in Fig. 10, with the data listed in Table S5. In Table S5, the total calculated binding energy for 1-OHP-BSA complex was (−17±4) kcal mol^{-1}. The difference from the aforementioned experimental ΔG value (about -8.18 kcal mol^{-1}) was largely due to the ignorance of the entropy contributions in PBSA method. When the experimental ΔG also ignored the TΔS(-5.145 kal/mol) contribution, the calculated and experimental results were very close, indicating the accuracy of MM-PBSA method. In Fig. 10, the components of the binding free energy (ΔE_{bind}) show that the van der Waals energy (ΔE_{vdw}) makes the greatest contribution to the binding free energy, and the electrostatic energy (ΔE_{ele}) and the nonpolar solvation free energy ($\Delta E_{nonpolar}$) are also beneficial to the binding, while the polar solvation free energy (ΔE_{polar}) shows unfavorable contributions. In addition, compared to the value of sum of the polar interaction energies (ΣE_{polar}), the larger negative value of the sum of the nonpolar interaction energies ($\Sigma E_{nonpolar}$) indicated that the hydrophobic forces played the dominant role in stabilizing the binding of 1-OHP with BSA. This result is in agreement with that obtained from the experimental results. It is worth to note that the magnitude of ΔE_{ele} for the complex fluctuates greatly. Since hydrogen bonds between the ligand and protein are closely related to the electrostatic energy, the fluctuations of ΔE_{ele} are possibly related to the aforementioned formation and breakdown of the hydrogen bonds[34].

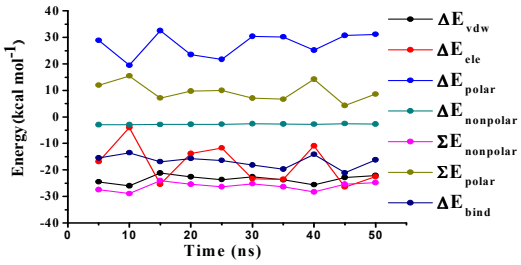

Fig. 10 Correlation of time span with the energy calculated using MM-PBSA. $\Sigma E_{polar}=\Delta E_{ele}+\Delta E_{polar}$, $\Sigma E_{nonpolar}=\Delta E_{vdw}+\Delta E_{nonpolar}$, $\Delta E_{bind}=\Delta E_{gas}+\Delta E_{sol}=(\Delta E_{vdw}+\Delta E_{ele})+(\Delta E_{polar}+\Delta E_{nonpolar})$

Key residue identification To further verify the contributions of each residue for binding free energy, the energy contribution difference analysis was performed. The polar and nonpolar contributions of 16 key residues with energies of absolute value no less than 0.15 kcal mol^{-1} were plotted in Fig. 11, with the data shown in Table S6. As can be seen, these key residues with strong contributions to the binding are all located in the Ⅰ B subdomain. Residues LYS116, LEU122, GLU140, ARG185 make strong contributions to the non-polar binding energy (red bar in Fig. 11), and contributes to the binding process. Whereas, LYS114, LEU115, ARG144, TRY160 and GLU182 make more contributions to the polar binding energy (blue bar in Fig. 11), and are unfavorable for the binding. For ARG185, although it contributes large values of van der Waals and aforementioned cation-π forces, the large penalty of solvation energy make ARG185 have a relative medium contribution to the binding process (Table S6). Instead, the non-polar residue PRO117 has strong hydrophobic contributions that overwhelmed the unfavorable polar interaction, and thus contributes most to the total binding energy, which indicates that PRO117 may be the strongest site to bind 1-OHP.

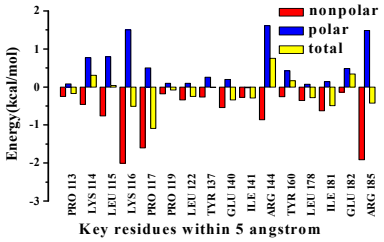

Fig. 11 Polar and nonpolar energy contributions for the key residues to the binding. Red bar: nonpolar energy ($\Delta E_{vdw}+\Delta E_{nonpolar}$); blue bar: Polar energy ($\Delta E_{ele}+\Delta E_{polar}$); yellow bar: total binding energy. Negative values are favorable and positive values are unfavorable for binding, polar or nopolar≥0.15.

Overall, the binding free energy decomposition results are consistent with the docking study and the experimental analysis. Combining the MD simulation, docking, and thermodynamic analysis, it is evidence that hydrophobic interaction, especially the van der Waals dominates the binding of 1-OHP to BSA, despite the existence of hydrogen bonds and electrostatic interactions.

Conclusions

This work regarding the combination of multi-spectroscopy and docking and MD methods has realized an in-depth understanding of not only the systematic interaction mechanism between 1-OHP and BSA but also the adverse effects of the binding on BSA. 1-OHP has been shown to form a strong 1:1 complex with BSA. Their quenching mechanism, binding constant, dominant binding forces and binding distance have been determined in a more realistic condition than the previous research reported by Ouyang et al [14]. The structural transitions and transport functional inhibition of BSA induced by the binding process are corroborated here. The specific binding location of 1-OHP in BSA and their dynamic binding mode have also been revealed and are visually represented. The stability of the 1-OHP-BSA complex is corroborated. The contributions of each interaction force to the binding process have been clarified. The key residues contributing most to the binding energy have also been verified. These results reveal the interaction mechanism of 1-OHP with BSA, and warn of the great potential toxicity of 1-OHP on the transport protein in organisms.

Besides, PAH metabolites can interact with other important biomacromolecules in vivo (e.g., glutathione peroxidase, catalase, superoxide dismutase, DNA, estrogen receptor, etc.), which can cause potential health hazards, such as oxidative damage, DNA damage, and endocrine disruption. Future work should be performed to further study the interactions of PAH metabolites

with these important targets based on the established methods, so as to help further understand the toxicity mechanism of PAH metabolites at both molecular and atomic level. Such insights are well worth extending to the toxicity assessment aspects of other environmental contaminants, emerging nanoparticles and drugs.

Acknowledgments

We gratefully acknowledge the financial support of the National Natural Science Foundation of China (No. 21075102, 21177102, 21577110) and the Xiamen University Innovative Research Foundation (No. DC2013035). We also thank the College of Pharmaceutical Sciences, Xiamen University and Department of Chemistry, College of Chemistry and Chemical Engineering, Xiamen University for providing us with the amber14 and Gaussian 09 software. We also express our thanks to Elsevier Language Editing Services for their assistance with English. We also thank the reviewers and editors for their suggestions that are very helpful in improving the quality of this work.

References

1 S. Augusto, C. Máguas, J. Matos, M. J. Pereira and C. Branquinho, Environ. Pollut., 2010, **158**, 483-489.
2 X. T. Wang, Y. Miao, Y. Zhang, Y. C. Li, M. H. Wu and G. Yu, Sci. Total Environ., 2013, **447**, 80-89.
3 G. Prodi, S. Grilli, M. Mazzullo, A. Colacci and G. Arfellini, Toxicol. Pathol., 1984, **12**, 185-188.
4 B. Moorthy, C. Chu and D. J. Carlin, Toxicol. sci., 2015, **145**, 5-15.
5 K. Yamasaki, V. T. G. Chuang, T. Maruyama and M. Otagiri, BBA-Gen. Subjects, 2013, **1830**, 5435-5443.
6 K. Skupińska, M. Zylm, I. Misiewicz and T. Kasprzycka-Guttman, Acta Biochim. Pol., 2006, **53**, 101-112.
7 Y. Y. Qin, C. K. M. Leung, C. K. Lin, A. O. W. Leung, H. S. Wang, J. P. Giesy and M. H. Wong, Environ. Sci. Technol., 2011, **45**, 1630-1637.
8 S. Naveenraj and S. Anandan, J. Photoch. Photobio. C, 2013, **14**, 53-71.
9 S. L. Zhuang, H. F. Wang, K. K. Ding, J. Y. Wang, L. M. Pan, Y. L. Lu, Q. J. Liu and C. L. Zhang, Chemosphere, 2016, **144**, 1050-1059.
10 Z. Q. Xu, Q. Q. Yang, J. Y. Lan, J. Q. Zhang, W. Peng, J. C. Jin, F. L. Jiang and Y. Liu, J. Hazard. Mater., 2016, **301**, 242-249.
11 A. M. Saletskii, A. G. Mel'Nikov, A. B. Pravdin, V. I. Kochubei and G. V. Meln'ikov, J. Appl. Spectrosc., 2008, **75**, 402-406.
12 P. Brunmark, S. Harriman, P. L. Skipper, J. S. Wishnok, S. Amin and S. R. Tannenbaum, Chem. res. toxicol., 1997, **10**, 880-886.
13 T. Q. Wu, Q. Wu, S. Y. Guan, H. X. Su and Z. J. Cai, Biomacromolecules, 2007, **8**, 1899-1906.
14 Y. Ouyang, Y. Wang and L. Guiying, Physical Testing and Chemical Analysis Part B: Chemical Analysis, 2011, **47**, 253-256.
15 R. T. Liu, W. S. Zong, K. Jin, X. T. Lu, J. H. Zhu, L. J. Zhang and C. Z. Gao, Spectrochim. Acta A., 2008, **70**, 198-200.
16 J. Zhang, W. X. Chen, W. Zhang, Y. Duan, Y. X. Zhu, Y. X. Zhu and Y. Zhang, Chem. J. Chinese U., 2015, **36**, 1511-1516.
17 C. B. Xu, J. L. Gu, X. P. Ma, T. Dong and X. L. Meng, Spectrochim. Acta A., 2014, **125**, 391-395.
18 D. Wu, Y. M. Zhai, J. Yan, K. L. Xu, Q. Wang, Y. Z. Li and H. Li, RSC Adv., 2015, **5**, 11036-11042.
19 F. Zhang, J. Zhang, C. L. Tong, Y. D. Chen, S. L. Zhuang and W. P. Liu, J. Hazard. Mater., 2013, **263**, 618-626.
20 L. F. Chen, J. Zhang, Y. X. Zhu and Y. Zhang, RSC Adv., 2015, **5**, 79874-79881.
21 J. Shen, W. Q. Zhang, H. Fang, R. Perkins, W. D. Tong and H. X. Hong, BMC bioinformatics, 2013, **14**, S6.
22 W. Peng, F. Ding and Y. K. Peng, Rsc Adv., 2016, **6**, 1826-1843.
23 L. F. Chen, J. Zhang, Y. X. Zhu and Y. Zhang, Chem. J. Chinese U., 2015, **36**, 2394-2401.
24 J. R. Lakowicz, Principles of fluorescence spectroscopy, third edition, Springer Science & Business Media, New York, 2006.
25 G. M. Morris, D. S. Goodsell, R. S. Halliday, R. Huey, W. E. Hart, R. K. Belew and A. J. Olson, J. comput. chem., 1998, **19**, 1639-1662.
26 M. Frisch, G. Trucks, H. B. Schlegel, G. Scuseria, M. Robb, J. Cheeseman, G. Scalmani, V. Barone, B. Mennucci and G. Petersson, Inc., Wallingford, CT, 2009, **200**.
27 A. Bujacz, Acta Crystallogr. D., 2012, **68**, 1278-1289.
28 A. Ganguly, B. K. Paul, S. Ghosh, S. Dalapati and N. Guchhait, Phys. Chem. Chem. Phys., 2014, **16**, 8465-8475.
29 W. L. DeLano, DeLano Scientific, San Carlos, CA, 2002, **452**.
30 D. A. Case, J. T. Berryman, R. M. Betz, D. S. Cerutti, T. E. Cheatham, III, T. A. Darden, R. E. Duke, T. J. Giese, H. Gohlke, A. W. Goetz, N. Homeyer, S. Izadi, P. Janowski, J. Kaus, A. Kovalenko, T. S. Lee, S. LeGrand, P. Li, T. Luchko, R. Luo, B. Madej, K. M. Merz, G. Monard, P. Needham, H. Nguyen, H. T. Nguyen, I. Omelyan, A. Onufriev, D. R. Roe, A. Roitberg, R. Salomon-Ferrer, C. L. Simmerling, W. Smith, J. Swails, R. C. Walker, J. Wang, R. M. Wolf, X. Wu, D. M. York and P. A. Kollman, University of California, San Francisco, 2015.
31 K. K. Ding, H. X. Zhang, H. F. Wang, X. Lv, L. M. Pan, W. J. Zhang and S. L. Zhuang, J. Hazard. Mater., 2015, **299**, 486-494.
32 J. Wang, R. M. Wolf, J. W. Caldwell, P. A. Kollman and D. A. Case, J. Comput. Chem., 2004, **25**, 1157-1174.
33 R. Ghadari, F. S. Alavi and M. Zahedi, Comput. Biol. Chem., 2015, **56**, 33-40.
34 F. C. Cui, K. C. Yang and Y. Q. Li, PLoS ONE, 2015, **10**, e0125848.
35 X. Peng, X. C. Wang, W. Qi, R. X. Su and Z. M. He, Food Chem., 2016, **192**, 178-187.
36 B. P. Pahari, S. Chaudhuri, S. Chakraborty and P. K. Sengupta, J. Phys. Chem. B, 2015, **119**, 2533-2545.
37 K. Lou, Z. H. Zhu, H. M. Zhang, Y. Q. Wang, X. J. Wang and J. Cao, Chem-Biol. Interact., 2016, **243**, 54-61.
38 N. A. Carmona, B. Cohen, J. A. Organero and A. Douhal, J. Photoch. Photobio. A., 2012, **234**, 3-11.
39 T. Tsukamoto and T. Hikida, J. Photochem. Photobiol. A-Chem., 1996, **95**, 271-273.
40 S. Endo and K. U. Goss, Chem. Res. Toxicol., 2011, **24**, 2293-2301.
41 P. D. Ross and S. Subramanian, Biochemistry, 1981, **20**, 3096-3102.
42 S. Huang, F. W. Zhu, Q. Xiao, Q. Zhou, W. Su, H. N. Qiu, B. Q. Hu, J. R. Sheng and C. S. Huang, Rsc Adv., 2014, **4**, 36286-36300.
43 X. R. Li and S. Wang, New J. Chem., 2015, **39**, 386-395.
44 T. Förster, Delocalized excitation and excitation transfer, Florida State University, 1965.
45 X. Peng, W. Qi, R. L. Huang, R. X. Su and Z. M. He, Plos One, 2015, **10(4)**, e0118274.
46 N. Tayeh, T. Rungassamy and J. R. Albani, J. Pharm. Biomed. Anal., 2009, **50**, 107-116.
47 O. S. Wolfbeis, M. Leiner, P. Hochmuth and H. Geiger, Ber. Bunsen-Ges. Phys. Chem. Chem. Phys., 1984, **88**, 759-767.

48 A. S. Sharma, S. Anandakumar, M. Ilanchelian and S. Anandakumar, Rsc Adv., 2014, **4**, 36267-36281.
49 X. Chen, K. Qian and Q. Chen, Eur. J. Med. Chem., 2015, **93**, 492-500.
50 Y. Z. Zhang, B. Zhou, Y. X. Liu, C. X. Zhou, X. L. Ding and Y. Liu, J. fluoresc., 2008, **18**, 109-118.
51 C. Jash and G. S. Kumar, RSC Adv., 2014, **4**, 12514-12525.
52 S. Huang, H. N. Qiu, S. Y. Lu, F. W. Zhu and Q. Xiao, J. Hazard. Mater., 2015, **285**, 18-26.
53 N. J. Greenfield, Nat. protoc., 2006, **1**, 2876-2890.
54 X. Y. Xie, W. J. Lü and X. G. Chen, J. Hazard. Mater., 2013, **248**, 347-354.
55 F. Chiti and C. M. Dobson, Annu. Rev. Biochem., 2006, **75**, 333-366.
56 Y. Shu, W. W. Xue, X. Y. Xu, Z. M. Jia, X. J. Yao, S. W. Liu and L. H. Liu, Food Chem., 2015, **173**, 31-37.
57 X. J. Guo, X. D. Sun and S. K. Xu, J. Mol. Struct., 2009, **931**, 55-59.
58 H. W. Zhao, M. Ge, Z. X. Zhang, W. F. Wang and G. Z. Wu, Spectrochim. Acta A., 2006, **65**, 811-817.
59 M. Voicescu, D. G. Angelescu, S. Ionescu and V. S. Teodorescu, J. Nanopart. Res., 2013, **15**, 1-10.
60 F. Wang, W. Huang and Z. X. Dai, J. Mol. Struct., 2008, **875**, 509-514.
61 X. Zhang, L. Chen, X. C. Fei, Y. S. Ma and H. W. Gao, BMC mol. biol., 2009, **10**, 16.
62 J. B. Chen, X. F. Zhou, Y. L. Zhang, Y. J. Qian and H. P. Gao, Amino Acids, 2012, **43**, 1419-1429.
63 S. Neelam, M. Gokara, B. Sudhamalla, D. G. Amooru and R. Subramanyam, J. Phys. Chem. B, 2010, **114**, 3005-3012.
64 A. Selva Sharma, S. Anandakumar and M. Ilanchelian, J. Lumin., 2014, **151**, 206-218.
65 F. Zsila, Mol. pharm., 2013, **10**, 1668-1682.
66 H. Z. Shen, Y. Huang, R. Wang, D. Zhu, W. Li, G. F. Shen, B. Wang, Y. Y. Zhang, Y. C. Chen, Y. Lu, H. Chen, T. C. Li, K. Sun, B. G. Li, W. X. Liu, J. F. Liu and S. Tao. Environ. sci. technol., 2013, **47**, 6415-6424.
67 M. Shahlaei, B. Rahimi, M. R. Ashrafi-Kooshk, K. Sadrjavadi and R. Khodarahmi, J. Lumin., 2015, **158**, 91-98.
68 S. Y. Liao, G. Q. Mo, J. C. Chen and K. C. Zheng, J. Mol. Model., 2014, **20**, 1-9.

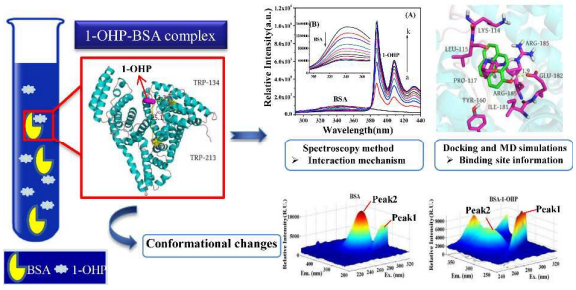

Combining multi-spectroscopy, docking with MD simulations, the interactions of 1-hydroxypyrene with BSA and the adverse effects on BSA were investigated.